ISSN (Print) 1226-1750
ISSN (Online) 2233-6656
Journal of Magnetics 25(1), 36-42 (2020) https://doi.org/10.4283/JMAG.2020.25.1.036

Crystal Structure and Magnetic Properties of Co-Mo Alloys Produced by Mechanical Alloying

J. A. Betancourt-Cantera[1]*, A. M. Bolarín-Miró[2], F. Sánchez-De Jesús[2], and L. G. Betancourt-Cantera[2]

[1]*CONACYT-Corporación Mexicana de Investigación en Materiales, Ciencia y Tecnología # 790, Col. Saltillo 400, CP 25290. Saltillo, Coahuila, México*
[2]*Área Académica de Ciencias de la Tierra y Materiales, UAEH, Carr. Pachuca-Tulancingo Km. 4.5, Pachuca, Hidalgo, 42184, México*

(Received 2 January 2020, Received in final form 25 March 2020, Accepted 25 March 2020)

We report the analysis of the crystal structure and the magnetic properties of $Co_{100-X}Mo_X$ alloys ($0 < x < 100$, $\Delta x = 10$), obtained by mechanical alloying using a shaker mixer mill, at room temperature for 7 h. Crystal structure, morphology and magnetic properties of the Co-Mo system were characterized through XRD (X-ray diffraction), SEM (scanning electron microscopy) and VSM (vibrating sample magnetometry). The results showed different completely soluble solid solution, in almost all compositions. Williamson-Hall method revealed an increase in the crystallite size, decreased with the molybdenum content, from 27.34 nm to 8.02 nm for 0 to 100 wt.% of Mo, respectively. Saturation magnetization and the magnetocrystalline anisotropy, showed the same behavior, a diminution with the increase of the molybdenum content. However, the coercivity increased with the increment in Mo content, reaching a maximum of 63.79 kA/m for $Co_{20}Mo_{80}$.

Keywords : mechanical alloying, Co-Mo alloys, crystal structure, magnetic properties, magnetocrystalline anisotropy

1. Introduction

Cobalt-based alloys have been used since the early 20th century for its interesting technical properties [1]. There is a wide variety of cobalt-based materials available on the market, showing different microstructural features and mechanical properties [2]. Their applications are very important in different areas, due to they have excellent physical, chemical and mechanical properties, such as superior fatigue resistance, wear resistance, corrosion resistance [3], resistant to heat (high strength even at high temperatures) [4], and good biocompatibility [5-8], among others. Some researchers have discussed the cobalt-based alloys applications in devices such as batteries, cemented carbide, stainless steel, petrochemical, automobile manufacturing, machine tools, hard metals, superalloys, gas turbine components, industrial catalysts, biomaterials, intravascular stent material, vanes and metallic orthopedic implants, radiofrequency devices, magnetic sensors and medical diagnosis [9-16]. Some of these Co-base alloys generally are formed by transition metals, which exhibit different properties, such as high hardness and strength, usually good conductors of heat and electricity [17] or exhibiting ferromagnetic properties [18].

Co-based alloys show a precipitation hardening effect when further elements such as molybdenum are added [19-21]. The molybdenum is a transition metal and has a body-centered cubic (bcc) crystal lattice. This element has been added in small amounts in several alloys for hardening, and at the same time, it increases the corrosion resistant, in according to Bazaglia *et al.* [22].

Molybdenum is classified as a refractory metal with high melting temperature, high density, high stiffness, high-temperature strength, and low thermal expansion [23-25]. On the other hand, the magnetic properties of cobalt can be modified by the addition of molybdenum. The presence of molybdenum in the composition of cobalt alloys, reduces the grain size, thus enhances the strengthening of solid solution and subsequently improves the mechanical properties of these alloys [26, 27]. Besides, the introduction of molybdenum in the cobalt-nickel alloy can be tested as a method of decreasing the coercitivity, maintaining high values of saturation magnetization according to Gomez [28].

Over time, different methods to obtain alloys Co-Mo have been applied, such as electrodeposition [28], melting

*Corresponding author: Tel: +52-771-279-8021
Fax: +52-844-416-2679, e-mail: jbetancourt@comimsa.com

[22] and powder bed fusion [19]. Among others, mechanical alloying (MA) is one of the most effective and economical methods to produce powders with nano-sized structure, such as have been demonstrated in different studies [29, 30]. During powder milling, the particles are undergone high-energy impacts by balls. The high-energy impacts result in a high amount of defects such as vacancies, dislocations, grain boundaries and stacking faults in particles which in turn give rise to nanometer crystallite size and phase transformations [31]. The MA (mechanical alloying) can be used to produce alloys, metastable intermetallic compound, and the amorphous phase that are difficult or impossible to obtain by conventional melting and casting methods [32]. As it is known, the mechanical properties are significantly affected by phases constituent, grain size, grain morphology, and the characteristics of precipitates. Furthermore, in Co-based alloys, refinement of grain sizes can enhance the tensile strength, and augment of ε phase, increasing the hardness but decreasing the ductility, in according to Saldivar and Wei [33, 34].

In this work, a study of Co-Mo alloys was done in order to find correlations between the crystal structure and the magnetic properties, as a function of the molybdenum content and, the effects produced by the milling process.

2. Materials and Experimental Procedures

Elemental cobalt powder (> 99.9% purity from Sigma-Aldrich), with a mean particle size (D_{50}) of 10 μm and, elemental molybdenum powder > 99.9% purity from Sigma-Aldrich) with a mean particle size (D_{50}) of 22.5 μm were used as precursors. A total amount of 5 g of powder mixture with 6 hardened steel balls with a diameter of 12.7 mm were loaded into a steel vial with 64.6 cm^3 of volume and milled for 7 h. The mechanical alloying process was conducted at room temperature in an argon atmosphere, using a SPEX 8000D shaker mill. The ball-to-powder weight ratio was 12:1. The raw materials were mixed in the appropriate weight ratio to obtain $Co_{100-X}Mo_X$ where x varies from 10 to 90 wt.%.

The milled powders were analyzed by X-ray diffraction (XRD) for examining the phase transformations as a function of the alloy composition, using a Siemens D5000 diffractometer. The diffraction parameters were collected with 2θ ranging from 35° to 120° with a step size of 0.02 and Co K_α ($\lambda = 1.7902$ Å) radiation. Rietveld refinement was performed on the X-ray diffraction patterns using the program MAUD [35]. The crystallite size (D) in the milled samples was calculated from the XRD line broadening using the Williamson-Hall method [36].

The magnetic properties of the obtained materials, specific saturation magnetization (M_S) and coercivity (H_C), were measured using a LDJ9600 vibrating magnetometer (VSM) with a maximum applied field of 15 kOe. Morphological characterization of the milled powders was performed using a Leica Stereoscan 440 electron microscope operated at 20 kV. The magnetic anisotropy constant was determined for each composition using the law of approach to saturation [37].

3. Results and Discussion

3.1. Structural Analysis

Figure 1 shows the XRD patterns of $Co_{100-X}Mo_X$ ($10 < x < 100$, $\Delta x = 10$) powders, as a function of the molybdenum content (x, as weight percent), milled for 7 h. In Fig. 1 is included the XRD pattern corresponding to the elemental Co powder, without milling. It confirms that the pure Co presents two phases, hexagonal Co-ε (PDF # 05-0727, *P63/mmc*, hcp) and cubic Co-α (PDF # 15-0806, *Fm-3m*, fcc). In contrast, the XRD corresponding to elemental Mo shows a single cubic phase, Mo-bcc (ICDD # 03-065-7442, *Im-3m*, bcc).

When the powder is mixed and milled for 7 h, the XRD patterns corresponding to the composition with x varying from 10 to 30 wt.% ($Co_{90}Mo_{10}$, $Co_{80}Mo_{20}$ and $Co_{70}Mo_{30}$) shows a mixture of Co(Mo)-fcc, Co(Mo)-hcp and Mo(Co)-bcc (partial solid solutions). It can be seen that the diffusion of cobalt occurs toward the structure of molybdenum, increasing the relative intensity of to the main peak (1 1 0) at 48° of 2θ (marked with dash dot line in Fig. 1). Besides, the broadening of the main peaks of cobalt and molybdenum are visualized; this effect is a consequence of the energy storage, the structural defects, the particle size reduction, and the accumulation of stacking faults induced during mechanical alloying, according to other works [38-44]. On the other hand, the peak (0 0 2) corresponding to the hcp-Co phase is observed, as a result of an allotropic transformation of Co from fcc phase to hcp structure, according to the reported in previous works [45]. For higher molybdenum contents (x = 40, 50, 60 wt.%) it can be observed the same behavior, only is detected an increase in the relative intensity of the Mo (1 1 0) diffraction peak and, a progressive diminution of the Co-hcp peaks, attributed to the formation of solid solutions.

For high molybdenum contents, x values from 70 to 90 ($Co_{30}Mo_{70}$ and $Co_{10}Mo_{90}$) the results confirm that cobalt is introduced into the molybdenum cubic structure. The presence of bcc-Mo phase can be depicted clearly in the XRD, confirmed by the reflection peaks at 47.42°, 69.3° and 88.28° of 2θ. The diffraction patterns show that there

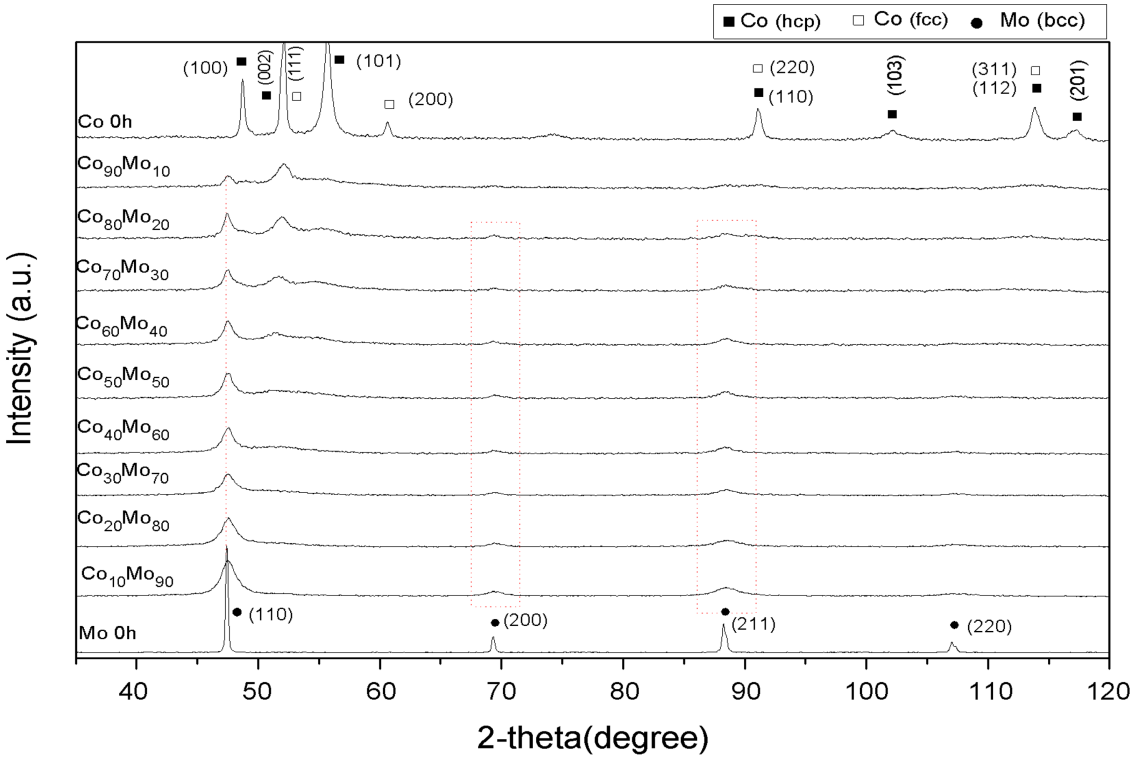

Fig. 1. (Color online) XRD patterns of $Co_{100-X}Mo_X$ samples with x 10 to 90 ($\Delta x = 10$) milled for 7 h.

are no peaks from pure Co, and only the (1 1 0), (2 0 0) and (2 1 1) reflections, corresponding to Mo are present, confirming the introduction of the cobalt atoms into the molybdenum structure.

In order to confirm the previous results, Rietveld refinements were done, using the XRD patterns shown in Fig. 1, the results are presented in Fig. 2. Fig. 2(a) and 2(b) display the refinement of $Co_{90}Mo_{10}$ and $Co_{60}Mo_{40}$,

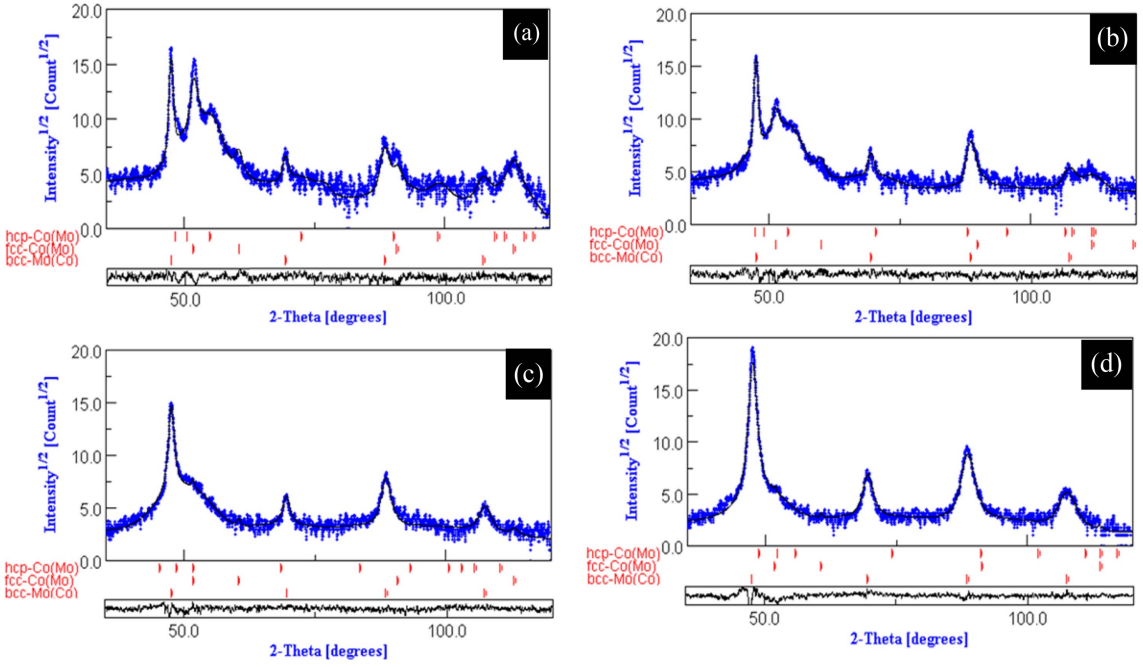

Fig. 2. (Color online) Rietveld refinements from (a) $Co_{90}Mo_{10}$, (b) $Co_{60}Mo_{40}$, (c) $Co_{40}Mo_{60}$ and (d) $Co_{10}Mo_{90}$ compositions.

respectively. As can be observed, the Co-fcc diffractions peaks decrease their intensities, due to the partial transformation to hcp-Co, and the main diffraction peak of the Mo are still present, because of Mo is not soluble in the Co crystal structure. In addition, the Rietveld refinement $Co_{40}Mo_{60}$ composition, displayed in Fig. 2(c), shows the same behavior, but in this case, it is observed a decrease of the intensity of the main peak of cobalt, as a consequence of the partial introduction of the cobalt into the cubic structure of molybdenum. Finally, in Fig. 2(d), where is presented the Rietveld refinement of the composition $Co_{10}Mo_{90}$, it is confirmed the complete solid solution of Co into the bcc-Mo, due to only the diffraction peaks of molybdenum are detected. For all the studied compositions, the broad of peaks can be related with structural defects introduced during the mechanical milling, such as has been reported in previous works [32, 40, 41].

To quantify the obtained phase and the structural modifications, in Table 1 are presented parameters such as phase and percentage of each phase, crystallite size, and particle diameter (Dm_{50}). Such as discussed in XRD, three phases were obtained, in all milled compositions (Co(Mo)-hcp, Co(Mo)-fcc and Mo(Co)-bcc) and their percentages are displayed in Table 1, showing the evolution of each phase in different compositions. It's observed the increases in the amount of Mo(Co)-bcc from 8.49 ± 0.12 % to 100 %, for $Co_{90}Mo_{10}$ and $Co_{10}Mo_{90}$, respectively. Moreover, the diminishes of Co(Mo)-hcp percentages from 78.83 ± 0.30 % to 2.54 ± 0.15 % and for Co(Mo)-fcc from 12.68 ± 0.08 % to 1.98 ± 0.05 % for the compositions $Co_{90}Mo_{10}$ and $Co_{40}Mo_{60}$, respectively. In reference to the crystal size, as can be appreciated in Table 1, there is a progressive decrement of the crystallite size as the molybdenum content is increased, from 27.34 nm to 8.02 nm, for $Co_{90}Mo_{10}$ and $Co_{30}Mo_{70}$, respectively. The reduction of the crystallite size is induced by a diminution of the grain size, generated by the high-energy ball milling. After, there are a slight recovery from 8.02 nm to 12.96 nm for the composition $Co_{10}Mo_{90}$, this behavior can be associated with the presence of Mo(Co)-bcc phase, attributed to the generation of dislocations, caused by severe plastic deformation during the high-energy milling process.

Table 1. Phases and % of each composition, crystal size and particle diameter (Dm_{50}), as a function of the molybdenum content.

Composition Co_{100-X}-Mo_X	Phases and % for each composition	Crystal Size (nm).	Particle diameter (Dm_{50}) in μm.
	Co(Mo)-hcp 78.83 ± 0.30 %		
$Co_{90}Mo_{10}$	Co(Mo)-fcc 12.68 ± 0.08 %	27.34	33.12
	Mo(Co)-bcc 8.49 ± 0.12 %		
	Co(Mo)-hcp 69.55 ± 0.13 %		
$Co_{80}Mo_{20}$	Co(Mo)-fcc 18.51 ± 0.32 %	24.92	24.95
	Mo(Co)-bcc 11.94 ± 0.21 %		
	Co(Mo)-hcp 51.81 ± 0.18 %		
$Co_{70}Mo_{30}$	Co(Mo)-fcc 14.15 ± 0.22 %	24.81	18.86
	Mo(Co)-bcc 34.04 ± 0.15 %		
	Co(Mo)-hcp 33.38 ± 0.08 %		
$Co_{60}Mo_{40}$	Co(Mo)-fcc 11.94 ± 0.16 %	13.04	12.99
	Mo(Co)-bcc 54.68 ± 0.36 %		
	Co(Mo)-hcp 15.59 ± 0.23 %		
$Co_{50}Mo_{50}$	Co(Mo)-fcc 3.85 ± 0.04 %	12.75	12.85
	Mo(Co)-bcc 80.56 ± 0.32 %		
	Co(Mo)-hcp 2.54 ± 0.15 %		
$Co_{40}Mo_{60}$	Co(Mo)-fcc 1.98 ± 0.05 %	12.07	11.83
	Mo(Co)-bcc 95.48 ± 0.07 %		
$Co_{30}Mo_{70}$	Mo(Co)-bcc 100 %	8.02	8.94
$Co_{20}Mo_{80}$	Mo(Co)-bcc 100 %	10.85	7.45
$Co_{10}Mo_{90}$	Mo(Co)-bcc 100 %	12.96	7.42

Figure 3 shows the SEM micrographs for the different compositions. It is observed a large increase in particle size with the cobalt content, due to the formation of agglomerates with irregular shape, from 15 μm to 43 μm. It is a result of the cold welding, caused by the milling process (Fig. 3(a)). The large particle size (marked with red arrows) in high cobalt alloys is attributed to the high ductility of the elemental cobalt, which tends to form agglomerates through cold welding between particles. When the molybdenum content is increased up to x = 30 and 50 wt.% (Fig. 3(b) and 3(c)), the agglomerates show a slight reduction with respect to the sample $Co_{90}Mo_{10}$, because of Mo which is a brittle material, limits the cold welding between Co particles, due to it is located between Co particles. This reduction in the particle size, with the increase in Mo content, is accompanied with a change in the shape of the particles, as well as a decrease in the size of the agglomerates, from 5 μm to 10 μm, yielding smaller particle sizes.

To corroborate this assertion, in Table 1 is shown particle diameter (Dm_{50}). The results are consistent with the micrographs presented in Fig. 3. It is presented a particle size reduction, from 33.12 μm to 7.42 μm, increasing the molybdenum content for $Co_{90}Mo_{10}$ and $Co_{10}Mo_{90}$ respectively. In addition, when a solid solution of Mo-bcc has been obtained (from $Co_{30}Mo_{70}$ to $Co_{10}Mo_{90}$) it can be observed a homogeneous particle size.

3.2. Magnetic Characterization

Figure 4 shows the hysteresis magnetic loops (*M-H*) for $Co_{100-x}Mo_x$ alloys ($10 < x < 90$). Here, it is remarkable

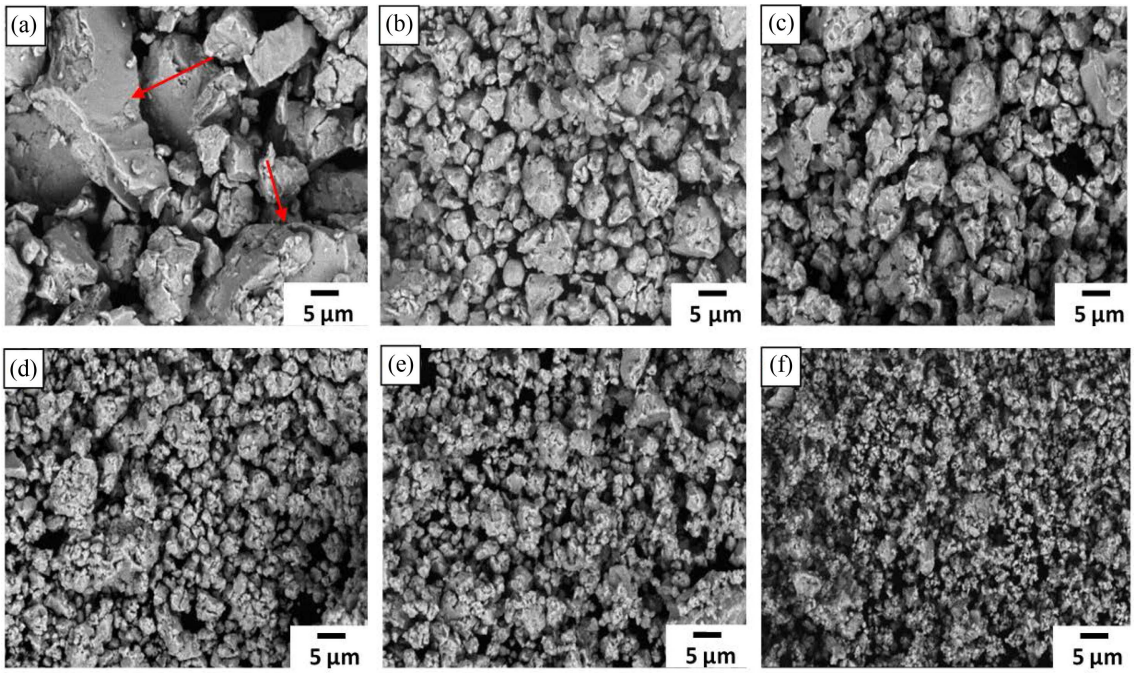

Fig. 3. (Color online) SEM micrographs for different compositions: (a) $Co_{90}Mo_{10}$, (b) $Co_{70}Mo_{30}$, (c) $Co_{50}Mo_{50}$, (d) $Co_{30}Mo_{70}$, (e) $Co_{20}Mo_{80}$, (f) $Co_{10}Mo_{90}$.

Table 2. Saturation magnetization, coercivity field and magnetocrystalline anisotropy constant, as a function of the molybdenum content.

Composition Co_{100-X}-Mo_X	Ms (Am^2/kg)	Hc (kA/m)	K_1 ($\times 10^5$ J/m^3)
$Co_{90}Mo_{10}$	143.58	20.85	3.80
$Co_{80}Mo_{20}$	119.99	27.55	2.73
$Co_{70}Mo_{30}$	84.48	28.88	1.23
$Co_{60}Mo_{40}$	48.39	26.29	0.44
$Co_{50}Mo_{50}$	26.78	27.78	0.31
$Co_{40}Mo_{60}$	4.52	38.26	0.06
$Co_{30}Mo_{70}$	2.61	59.24	0.02
$Co_{20}Mo_{80}$	4.23	63.79	0.03
$Co_{10}Mo_{90}$	6.21	54.71	0.06

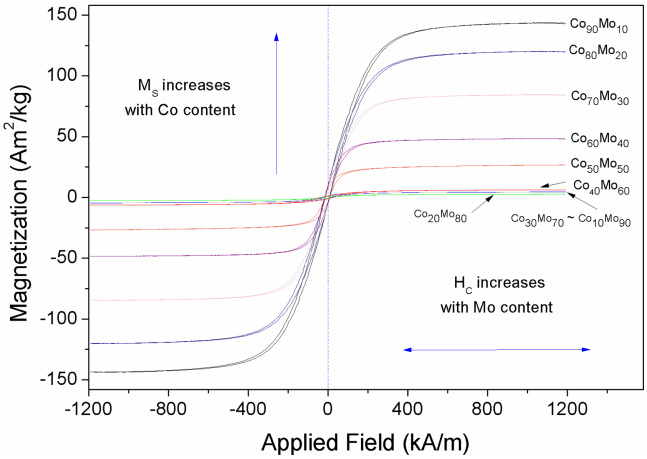

Fig. 4. (Color online) Hysteresis loops for $Co_{100-X}Mo_X$ system for different values of *x*.

that all the compositions show a ferromagnetic behavior with low coercivity, representative of soft magnetic materials. In order to analyze some of the magnetic properties of the milled powder, in Table 2, the magnetic parameters, such as saturation magnetization, M_S, coercivity, H_C and, magnetocrystalline anisotropy constant K_1, versus the composition of Mo in wt.%, are presented.

As can be observed, M_S decreases drastically with the increase of the molybdenum content, from 143.58 Am^2/kg for $Co_{90}Mo_{10}$ to 2.61 Am^2/kg for $Co_{30}Mo_{70}$, as shown in Fig. 4. This noticeable decrease of M_S can be attributed to the dilution effect of the magnetic moment of cobalt atoms promoted by the formation of the Co(Mo) and Mo(Co) solid solutions (structural changes), i.e., the diminution of the Co(Mo) hcp and fcc phases amounts, displayed in Table 1. Also, the increase of the molybdenum content that promotes the competition between ferromagnetic (Co) and paramagnetic (Mo) exchange interactions [44]. Finally, for the $Co_{20}Mo_{80}$ and $Co_{10}Mo_{90}$, the M_S exhibits a slightly increment from 4.23 Am^2/kg and 6.21 Am^2/kg respectively, respect to $Co_{30}Mo_{70}$. The change of *Ms* observed in Co-Mo system is due to the formation of bcc-Mo(Co) total solid solutions, and fcc-

Co(Mo), hcp-Co(Mo), bcc-Mo(Co) partial solid solutions obtained in all compositions, as a consequence of the increment of the molybdenum content. The percentages of each phase are shown in Table 1.

Furthermore, the coercivity behavior is showed in Table 2, where is observed a tendency to increase from 20.85 kA/m to 63.79 kA/m for $Co_{90}Mo_{10}$ to $Co_{20}Mo_{80}$, respectively, then it falls up to 54.71 kA/m for compositions of 90 % of molybdenum. The H_C is one of the microstructure sensitive magnetic properties of materials, because of, the coercivity is an extrinsic property that strongly depends on the internal defects such as reduction in grain size, residual stresses, grain boundaries and non-magnetic inclusions (dislocations and inclusion of additional materials) [45, 46]. The increase in H_C can be correlated to the induced magnetic anisotropy and change in the grain boundaries, which acts as inclusions hindering the domain wall motion [47].

Moreover, the magnetocrystalline anisotropy constant K_1 data, are presented in Table 2, it can be observed that K_1 tends to reduce as the % of cobalt (in wt.) decreases, it is noted the reduction from 3.8×10^5 J/m^3 for $Co_{90}Mo_{10}$ composition to 0.02×10^5 J/m^3 for $Co_{30}Mo_{70}$ composition. This general tendency for reduction in K_1, is attributed to the effect of the reduction in crystallite size, which reduces the magnetocrystalline anisotropy.

For the compositions $Co_{20}Mo_{80}$ and $Co_{10}Mo_{90}$, a slight recovery in K_1 is noted with 0.04×10^5 J/m^3 and 0.06×10^5 J/m^3 respectively, this behavior is related to the increase of the crystallite size. Furthermore, in accordance with Toparlia *et al.* [48], this behavior can be explained by many factors such as crystallite size, crystallinity, defects, pores and surface anisotropy affect. However, it is mainly affected by the critical crystallite size.

4. Conclusion

Mechanical alloying promotes solid solution formation and grain size refinement of $Co_{100-X}Mo_X$ alloys. The saturation magnetization, M_S, decreases from 143.58 Am^2/kg to 2.61 Am^2/kg for 10 and 70 wt.% of Mo, respectively. It is attributed to the formation of solid solution based Mo-bcc. It promotes a competition between ferromagnetic and paramagnetic exchange interactions. Coercivity, H_C, increases from 20.85 kA/m to 63.79 kA/m for 10 and 80 wt.% of Mo. On the other hand, the magnetocrystalline anisotropy is reduced from 3.8×10^5 J/m^3 to 0.02×10^5 J/m^3 for 10 and 70 wt.% of Mo, due to the Mo promotes the reduction in crystallite size. In consequence, the reduction in the magnetocrystalline anisotropy is caused by the average effect of magnetization over the randomly oriented nano-sized grains.

Acknowledgements

The authors acknowledge research support from CONACyT from México and Cátedras CONACyT with the following ID number: 2362.

References

[1] L. H. M. Antunes and C. R. P. de Lima, Ref Module Mater Sci. Mater. Eng. (2018).
[2] Q. Chen and G. A. Thouas, Mater. Sci. Eng. R **87**, 1 (2015).
[3] J. L. Acevedo-Dávila, R. Muñoz-Arroyo, H. M. Hdz-García, A. I. Martínez-Enríquez, M. Álvarez-Vera, and F. A. Hernández-García, Vacuum **143**, 14 (2017).
[4] M. Álvarez-Vera, A. Hernández-Rodríguez, M. A. L. Hernández-Rodríguez, A. Juárez Hernández, J. R. Benavides-Treviño, and J. H. García-Duarte, METABK **55**, 3 (2016).
[5] D. Coutsouradis, A. Davin, and M. Lamberigts, Mater. Sci. Eng. **88**, 11 (1987).
[6] R. M. Rose, Materials for internal prostheses, Yearbook of Science and Technology, McGraw-Hill Book Co., New York (1974).
[7] T. M. Devine and J. Wulff, J. Biomed. Mater. Res. **9**, 2 (1975).
[8] M. Niinomi, Metall. Mater. Trans. A **33**, 477 (2002).
[9] I. Azcona, A. Ordóñez, J. M. Sánchez, and F. Castro, J. Mater Sci. **37**, 19 (2002).
[10] R. Sadanandam, M. F. Fonseca, K. Srikant, A. K. Sharma, S. K. Tangri, and A. K. Suri, Hydrometallurgy **91**, 1 (2008).
[11] Y. Liu, Y. Zhu, Y. Zhang, Y. Qian, M. Zhang, L. Yang, and C. Wang, J. Mater. Chem. **7**, 5 (1997).
[12] X. Xi, Z. Nie, K. Xu, L. Ma, G. Chen, X. Zhang, and T. Zuo, Int. J. Refract. Met. Hard Mater. **41**, 90 (2013).
[13] A. L. Rominiyi, M. B. Shongwe, and B. J. Babalola, IOP Conf. Ser.: Mater. Sci. Eng. **430**, 012029 (2018).
[14] F. Sánchez-De Jesús, A. M. Bolarín-Miró, G. Torres-Villaseñor, C. A. Cortés-Escobedo, and J. A. Betancourt-Cantera, J. Mater. Sci. **21**, 7 (2010).
[15] Q. Wang, Y. Ren, M. Babar Shahzad, W. Zhang, X. Pan, S. Zhang, and D. Zhang, Mater Sci Eng: C **1**, 77 (2017).
[16] G. Srinivas, S. Ranjan, R. Prakash, and M. Jagannatham, Results Phys. **12**, 652 (2019).
[17] D. Moszyński, Int. J. Refract. Met. Hard Mater. **41**, 449 (2013).
[18] M. Kim, J. Magn. **21**, 1 (2016).
[19] E. Santecchia, A. Gatto, E. Bassoli, L. Denti, B. Rutkowski, P. Mengucci, and G. Barucca, J. Alloys Compd. **797** (2019).
[20] T. Matković, P. Matković, and M. Jadranka, J. Alloys Compd. **366**, 1 (2004).

[21] F. M. Yang, X. F. Sun, W. Zhang, Y. P. Kang, H. R. Guan, and Z. Q. Hu, Mater. Letter. **49**, 3 (2001).
[22] P. A. Bazaglia Kuroda, M. A. Rabelo Buzalaf, and C. R. Grandini, Mater. Sci. Eng. C **67**, 1 (2016).
[23] E. Lassner and W. D. Schubert, Tungsten: Properties, Chemistry, Technology of the Element, Alloys, and Chemical Compounds, Kluwer Academic/Plenum Publishers, New York (1999).
[24] T. Debroy, H. L. Wei, J. S. Zuback, T. Mukherjee, J. W. Elmer, J. O. Milewski, A. M. Beese, A. Wilson-Heid, A. De, and W. Zhang, Prog. Mater. Sci. **92**, 112 (2018).
[25] B. Cheng, Y.-J. Kim, and P. Chou, Nucl. Eng. Technol. **48**, 1 (2016).
[26] I. Milošev, CoCrMo alloy for biomedical applications in biomedical applications, In ed., Djokić, S., Biomedical Applications. Modern Aspects of Electrochemistry, vol 55. Springer, Boston, MA (2012) pp 1-72.
[27] H. A. Zaman, S. Sharif, D. W. Ki, M. H. Idris, M. A. Suhaimi, and Z. Tumurkhuyag, Procedia Manuf. **11**, 563 (2017).
[28] E. Gómez, E. Pellicer, and E. Vallés, J. Electroanal. Chem. **517**, 1 (2001).
[29] C. Song, H. Park, H. Seong, and H. F. Lopez, Metall. Mater. Trans. A **37**, 11 (2006).
[30] A. Mahboubi Soufiani, M. H. Enayati, and F. Karimzadeh, Mater. Des. **31**, 3954 (2010).
[31] M. Taghian Dehaghani, M. Ahmadian, and M. Fathi, Adv. Powder Technol. **25**, 6 (2014).
[32] J. A. Betancourt-Cantera, F. Sánchez-De Jesús, A. M. Bolarín-Miró, G. Torres-Villaseñor, and L. G. Betancourt-Cantera, J. Mater. Res. Technol. **8**, 5 (2019).
[33] A. de J. Saldívar, A. Maní, and A. Salinas, Metall. Mater. Trans. A **30**, 5 (1999).
[34] D. Wei, A. Anniyaer, Y. Koizumi, K. Aoyagi, M. Nagasako, H. Kato, and A. Chiba, Addit. Manuf. **28**, 215 (2019).
[35] L. Lutterotti, S. Matthies, and H. R. Wenk, MAUD: a friendly Java program for material analysis using diffraction, IUCr Newsletter of the CPD 21 (1999) pp 14-15.
[36] M. Khajepour and S. Sharafi, Powder Technol. **232**, 124 (2012).
[37] S. V. Andreev, M. I. Bartashevich, V. I. Pushkarsky, V. N. Maltsev, L. A. Pamyatnykh, E. N. Tarasov, N. V. Kudrevatykh, and T. Goto, J. Alloys Compd. **260**, 196 (1997).
[38] S. Louidi, F. Z. Bentayeb, W. Tebib, J. J. Suñol, L. Escoda, and A. M. Mercier, J. Alloys Compd. **536**, S1 (2012).
[39] F. Z. Bentayeb, S. Alleg, and J. M. Grenéche, J. Alloys Compd. **434-435**, 477 (2007).
[40] F. Sánchez-De Jesús, A. M. Bolarín-Miro, G. Torres-Villaseñor, C. A. Cortés-Escobedo, and J. A. Betancourt-Cantera, J. Mater. Sci. Mater. Med. **21**, 2021 (2010).
[41] J. A. Betancourt-Cantera, F. Sánchez-De Jesús, G. Torres-Villaseñor, A. M. Bolarín-Miró, and C. A. Cortés-Escobedo, J. Alloys Compd. **529**, 58 (2012).
[42] H. Moumeni, A. Nemamcha, S. Alleg, and J. M. Grenéche, Mater. Chem. Phys. **122**, 439 (2010).
[43] J. Y. Huang, Y. K. Wu, and H. Q. Ye, Acta Mater. **44**, 1201 (1996).
[44] S. Louidi, F. Z. Bentayeb, W. Tebib, J. J. Suñol, L. Escoda, and A. M. Mercier, Chem. Phys. **132**, 761 (2012).
[44] Z. Hua, Y. M. Sun, W. Q. Yu, M. B. Wei, and L. H. Liu, J. Alloys Compd. **477**, 529 (2009).
[45] J. A. Betancourt-Cantera, F. Sanchez-De Jesús, A. M. Bolarín-Miró, I. Betancourt, and G. Torres-Villaseñor, J Magn. Magn. Mater. **354**, 178 (2014).
[46] P. C. Shyni and A. Perumal, J. Alloys Compd. **648**, 658 (2015).
[47] M. Khajepour and S. Sharafi, J. Alloys Compd. **509**, 29 (2011).
[48] C. Toparlia, B. Ebina, and S. Gürmen, J. Magn. Magn. Mater. **423**, 133 (2017).